



# Mechanisms and characterization of impact damage in 2D and 3D woven fiber-reinforced composites



Kevin R. Hart<sup>a,b</sup>, Patrick X.L. Chia<sup>a</sup>, Lawrence E. Sheridan<sup>a</sup>, Eric D. Wetzel<sup>c</sup>, Nancy R. Sottos<sup>b,d</sup>, Scott R. White<sup>a,b,\*</sup>

<sup>a</sup> Department of Aerospace Engineering, University of Illinois at Urbana-Champaign, 104 S. Wright St., Urbana, IL 61801, USA

<sup>b</sup> Beckman Institute for Advanced Science and Technology, University of Illinois at Urbana-Champaign, 405 N. Mathews Ave., Urbana, IL 61801, USA

<sup>c</sup> Weapons and Materials Research Directorate, U.S. Army Research Laboratory, RDRL-WMM-A, Bldg. 4600, Aberdeen Proving Ground, MD 21005, USA

<sup>d</sup> Department of Materials Science and Engineering, University of Illinois at Urbana-Champaign, 1304 W. Green St., Urbana, IL 61801, USA

## ARTICLE INFO

### Article history:

Received 4 January 2017

Received in revised form 30 June 2017

Accepted 2 July 2017

Available online 8 July 2017

### Keywords:

Impact behavior

Delamination

3-Dimensional reinforcement

## ABSTRACT

Low velocity impact damage of 2D and 3D woven glass/epoxy composites with the same areal density and material constituents were examined. Characterization of damage for both plate and beam sample geometries was investigated through the collection of high-resolution cross-sectional images after impact. Load and displacement data collected during impact testing reveals that the threshold load to introduce delamination damage is independent of the fabric architecture and is constant across a range of impact energies. Delamination length and opening of 3D woven composites was less than 2D composites impacted at the same energy as a result of suppression of delamination propagation and opening offered by the Z-tow reinforcement of the 3D fabric architecture. The formation of transverse shear cracks was independent of the fabric architecture.

© 2017 Elsevier Ltd. All rights reserved.

## 1. Introduction

Fiber reinforced composite materials are susceptible to low-velocity out-of-plane impact events that introduce internal structural damage in the form of inter-ply delamination, transverse matrix cracking, and tensile cracking [1]. This type of damage not only weakens the structure, but is difficult to detect because it occurs at relatively low impact energies and often leaves no visible indication on the material surface (i.e. barely visible impact damage, BVID). If this damage goes undetected it can slowly grow under alternating or fluctuating stress, leading to a loss in mechanical performance and potential failure [2].

It is well known that fiber architecture plays a significant role in damage formation and post-impact mechanical performance of impacted composite plates and beams. For example, composites with stacking sequences in which the angle variation from ply to ply is large show greater resistance to transverse and inter-ply crack propagation as a result of increased fiber bridging and crack deflection [3–9]. Composites made with woven fabrics have also

shown increased residual compressive strength and smaller delaminations than those made with unwoven unidirectional layers, though the differences are typically small [10]. Through thickness stitching and Z-pinning has also been employed to improve the critical energy release rates associated with fracture propagation. Mode I [11–17], mode II [18–22], and mixed mode fracture [23–25] tests show that critical energy release rates increased with increasing reinforcement until saturating above a critical density. In low-velocity impact studies, stitched and Z-pinned composites generally show similar maximum impact load and energy absorption when compared to similar unstitched composites. However, through thickness reinforcement (either via stitching or Z-pinning) reduces inter-ply delamination by providing additional energy dissipation mechanisms via crack deflection, fiber bridging, fiber pull out, and fiber rupture [1,26–28]. Despite the increased fracture performance, stitched and Z-pinned composites typically suffer decreased performance (tension, compression, flexure) with increasing stitch density due to fiber distortions which arise during manufacture of the preform [29].

More recently, three-dimensionally (3D) woven orthogonal non-crimp fabric architectures have been investigated for use in structural composite applications. 3D orthogonal weaving introduces through-thickness fiber tows which are co-woven with the in-plane tows allowing insertion through the fabric thickness

\* Corresponding author at: Department of Aerospace Engineering, University of Illinois at Urbana-Champaign, 104 S. Wright St., Urbana, IL 61801, USA.

E-mail address: [swhite@illinois.edu](mailto:swhite@illinois.edu) (S.R. White).

URL: <http://whitegroup.beckman.illinois.edu/> (S.R. White).

without rupturing in-plane fibers [30]. With the rise of this manufacturing innovation, there is significant debate regarding the benefits of 3D woven composites when compared to similar 2D woven structures. Despite multiple studies of the mechanical behavior of 3D woven composites in tension [31–35], compression [32], shear [32,36], and fatigue [37], there have been very few investigations directly comparing 3D to 2D. In 2010, Mouritz and Cox [29] consolidated current data on the in-plane mechanical properties of 3D woven, stitched, and pinned composites noting that it was difficult to compare properties of 3D orthogonal woven composites to equivalent 2D woven composites because data was scarce and many researchers failed to report areal densities and fiber volume fractions required for direct comparison. Data on the comparative low-velocity impact response of 2D and 3D woven composites is even more limited. Baucom et al. [38–40] looked at energy absorption and perforation in 2D and 3D woven composites of similar areal density over multiple impact events. Authors concluded that while energy absorption of the first few impact events were similar, 3D woven composites survived more strikes before perforation and absorbed more total energy because of the through thickness Z-tow binding. Unfortunately, damage size and characteristics were not recorded during this study.

In this paper, we compare impact response and damage formation for 2D and 3D woven composite plates and beams subject to out-of-plane, low-velocity impact. Specimens are identically fabricated by vacuum assisted resin transfer molding of glass/epoxy composites using woven preforms of the same areal density and material construct. Load and displacement data gathered during impact testing is analyzed to identify the onset of various damage modes. Post-impact fractography is employed to characterize the extent of damage including the length and separation of delaminations and the number of transverse shear cracks present. The effect of fiber architecture (2D vs. 3D) is revealed across a number of different damage metrics.

## 2. Materials and methods

### 2.1. Composite manufacture

Unit cells of the 2D and 3D woven composite architectures are depicted in Fig. 1. 3D woven composites were made from a single layer of 4.07 kg/m<sup>2</sup> (120 oz/yd<sup>2</sup>) S2-glass orthogonal weave fabric (Textile Engineering and Manufacturing) consisting of 3 warp and 4 weft layers held by a through thickness Z-tow travelling in the warp direction. The warp and weft directions contain 3.0 tows/cm and 2.7 tows/cm, respectively. 2D woven composites were made from 5 layers of 0.814 kg/m<sup>2</sup> (24 oz/yd<sup>2</sup>) 1.97 × 1.97 tows/cm (5 × 5 tows/in.) plain woven S2-glass fabric (Owens Corning Knytex SBA240F) arranged in a [0]<sub>5</sub> configuration, yielding the same fiber areal density (4.07 kg/m<sup>2</sup> = 5 × 0.814 kg/m<sup>2</sup>) as the 3D composites. Preforms were infused with epoxy resin by vacuum assisted resin transfer molding (VARTM). Epoxy resin components EPON 862 (diglycidyl ether of bisphenol F; Momentive, Inc.) and Epikure W (aromatic diamine; Momentive, Inc.) were obtained from Miller-Stephenson (Morton Grove, IL) and used as-received. Prior to infusion, components were mixed in a stoichiometric weight ratio of 100:26.4, heated for 30 min at 70 °C then degassed under vacuum for 2 h at 70 °C. VARTM infusion was carried out in a convection oven at 70 °C in order to lower the viscosity of the resin and facilitate wetting of the fabric during infusion. Immediately after infusion the sample was raised to 121 °C at 3 °C/min, held for 8 h, then cooled to room temperature at 1 °C/min. 2D woven composites yielded an average thickness of 3.07 ± 0.09 mm and fiber volume fraction of 52.2 ± 0.43% calculated by the matrix burn-off method [41]. 3D woven composites had an average thickness of 3.52 ± 0.06 mm and fiber volume fraction of 47.3 ± 0.24%. The lower fiber volume fraction in 3D woven samples is a result of interstitial regions present in the non-crimp orthogonally woven fiber preform which accommodate excess resin during infiltration.

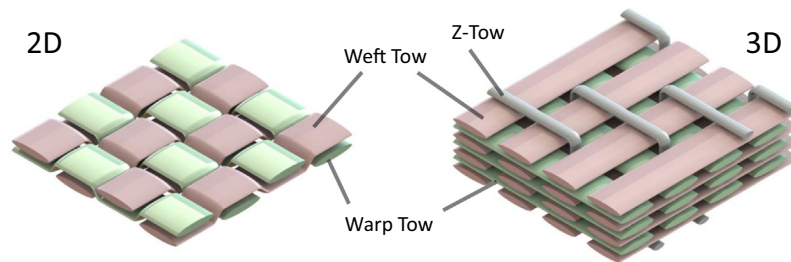


**Fig. 1.** Representative unit cells of 2D and 3D woven glass-fiber fabrics. The 2D fabric has an areal density of 814 g/m<sup>2</sup> and contains 2 tows/cm in both the warp and weft directions. The 3D fabric has an areal density of 4.07 kg/m<sup>2</sup> and contains 3 tows/cm in the warp direction and 2.7 tows/cm in the weft direction. (For interpretation of the references to colour in this figure legend, the reader is referred to the web version of this article.)

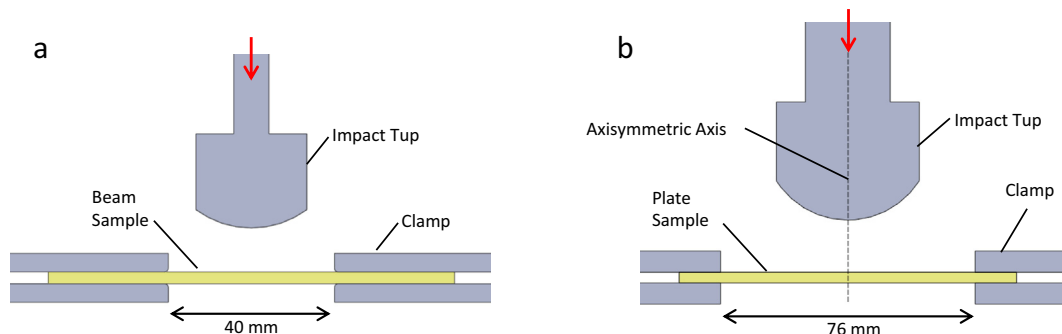


**Fig. 2.** Schematic of impact test configurations for composite beams and plates. (a) Cross-sectional view of a clamped beam sample prior to impact. Specimen is 20 mm in depth. (b) Cross-sectional view of a clamped plate sample prior to impact. Apparatus is axisymmetric about the annotated axis. Radius of curvature of both impact tups is 25.4 mm. (For interpretation of the references to colour in this figure legend, the reader is referred to the web version of this article.)

Plate samples were cut to  $101 \times 101$  mm to conform with ASTM D7137, the standard test method for compressive residual strength properties of damaged polymer matrix composite plates. Beam specimens were cut to  $20 \times 110$  mm with the warp direction aligned to the longitudinal axis of the beam to conform with ASTM D790, the standard test methods for flexural properties of unreinforced and reinforced plastics and electrical insulating materials.

## 2.2. Impact testing

### 2.2.1. Impact of beam specimens

Impact testing of beam samples was conducted on a drop-weight tower (Model 8250; Instron; Canton MA). Samples were clamped in a fixed-fixed configuration with a free span of 40 mm and impacted in the center of the span across the entire width of the specimen with a cylindrical impact tup (25.4 mm radius of curvature, Fig. 2a). The tup configuration and the range of impact energies used were selected to minimize fiber damage so that the effects of matrix damage and interface delamination alone could be isolated and investigated. Samples were impacted with a range of impact energies up to 25 J (Table 1). Load data was

collected during impact using a load cell (Model 8946-2; Instron) interfaced with LabVIEW (v 13.0) software. Acceleration, velocity, and displacement of the specimens were calculated assuming 1D impact dynamics (see Section S1 of SI).

### 2.2.2. Impact of plate specimens

Plate impact testing was conducted on a drop-weight tower (Dynatup 8200; Instron). Plate samples were circularly clamped (76 mm diameter free span) and impacted in the center with a hemi-spherically shaped impactor (25.4 mm radius of curvature, Fig. 2b). Samples were impacted with a range of energies up to 100 J (Table 2). Load data was collected during impact using a load cell (Model 8902-1; Instron) interfaced with LabVIEW (v 13.0) software. Acceleration, velocity, and displacement of the specimens were calculated assuming 1D impact dynamics (see Section S1 of SI).

### 2.2.3. Normalization of impact energy

To compare impact energy across plate and beam impact tests, impact energies were normalized by the unclamped volume of the sample during impact. For beams, this was calculated as:

**Table 1**

Impact testing conditions for composite beam specimens. Impact energies and impact velocities provided are theoretical values based on drop height and mass.

Fabric architecture	Drop height, mm	Drop mass, kg	Impact energy, J	Impact velocity, m/s	No. of samples
2D	152	3.36	5.01	1.73	8
	304	3.36	10.0	2.44	8
	455	3.36	15.0	2.99	8
	759	3.36	25.0	3.86	8
3D	152	3.36	5.01	1.73	8
	304	3.36	10.0	2.44	8
	455	3.36	15.0	2.99	8
	759	3.36	25.0	3.86	8

**Table 2**

Impact testing conditions for composite plate specimens. Impact energies and impact velocities provided are theoretical values based on drop height and mass.

Fabric architecture	Drop height, mm	Drop mass, kg	Impact Energy, J	Impact velocity, m/s	No. of samples
2D	600	4.34	25.5	3.43	8
	600	8.55	50.3	3.43	8
	600	12.79	75.3	3.43	8
	797	12.79	100	3.95	8
	600	4.34	25.5	3.43	8
3D	600	8.55	50.3	3.43	8
	600	12.79	75.3	3.43	8
	600	12.79	100	3.43	8
	797	12.79	100	3.95	8

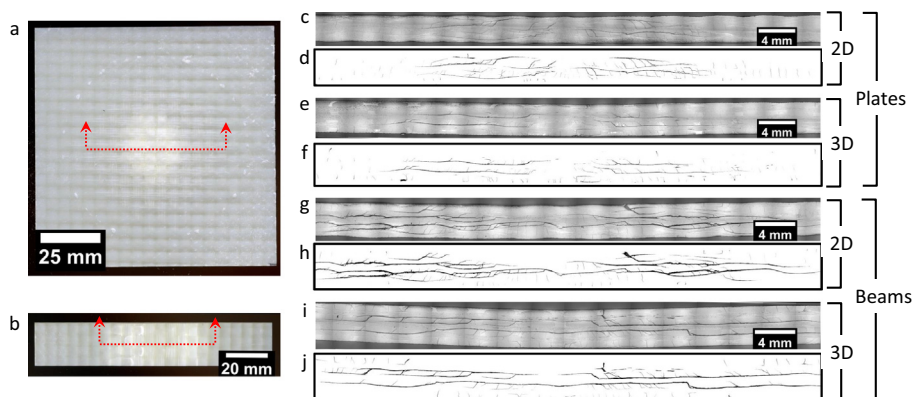


**Fig. 3.** Impact damage imaging and cross-sectional analysis. (a) Top view of composite plate impacted at 50.3 J. (b) Top view of composite beam impacted at 15.0 J. Red dashed line denotes cross-sectional imaging location. Optical micrographs and corresponding binary conversions of damaged composite cross-sections after impact: (c-f) 2D and 3D plate specimens impacted at 50.3 J, (g-j) 2D and 3D beam specimens impacted at 15.0 J. (For interpretation of the references to colour in this figure legend, the reader is referred to the web version of this article.)

$$\bar{U} = U/Lwt_{beam} \quad (1)$$

and for plates was calculated as:

$$\bar{U} = 4U/\pi D^2 t_{plate} \quad (2)$$

where  $\bar{U}$  is the impact energy density,  $U$  is the impact energy,  $L$  is the unclamped beam span,  $w$  is the beam width,  $t_{beam}$  is the beam thickness,  $t_{plate}$  is the plate thickness, and  $D$  is the unclamped diameter of the plate.

### 2.3. Cross-sectional imaging and damage characterization

Plate specimens were sectioned in half along the warp direction for standard analysis (Fig. 3a) or sectioned at angles of 30, 45, 60 or 90° with respect to the warp direction for axial-symmetry analysis. Beam specimens were sectioned in half along the longitudinal (warp) axis (Fig. 3b). Samples were then polished with successively finer grit paper and polishing compound until optically smooth (see detailed procedure in Section S2 of SI). Images of damaged samples were gathered in bright-field reflection using an optical microscope with a 2.5x objective (Axiovert 200M; Zeiss Corporation; Oberkochen, Germany) yielding 8-bit greyscale images with a resolution of 2.39  $\mu\text{m}/\text{pixel}$ . To view the entire cross-section, multiple images were stitched together using automatic image gathering and tiling options within the microscope control software (Axiovision 4.7; Zeiss Corporation). Measurement error

associated with the tiling process is considered negligible, the analysis of which is detailed in Section S3 of the SI.

Tiled cross-sectional images were analyzed using the counting, measuring, and classifying add-ons of Image Pro Plus software (v 7.0.1.658; Media Cybernetics, Inc.; Bethesda, MD). Fig. 4 depicts the analysis technique. After image collection, full-field 8-bit greyscale images (e.g. Fig. 4a) were converted to black and white binary images by implementing a half-scale intensity threshold filter (Fig. 4b). Adjoining groups of pixels were differentiated and groups of pixels with a combined area of less than 0.01 mm<sup>2</sup> were excluded from damage calculations by thresholding (Fig. 4c). The remaining continuous areas of pixels were then separated and individually categorized as a delamination or shear crack, manually, using a traced line split (Fig. 4d). An example image depicting groups of pixels classified as delaminations is provided in Fig. 4e.

Delamination length ( $L_d$ ) is defined as the maximum distance between any two pixels in a continuous grouping of delamination pixels. Total delamination length ( $\bar{L}_d$ ) is defined as the summation of all delamination lengths across all groups of pixels in a given cross-section. Delamination opening ( $A_d$ ) is defined as the sum of all pixels contained in a group of delamination pixels, multiplied by the calibrated area of a single pixel. Total delamination opening ( $\bar{A}_d$ ) is defined as the summation of all delamination openings across all groups of pixels in a given cross-section.

The number of transverse shear cracks occurring after impact was manually counted for each cross-section. Damage

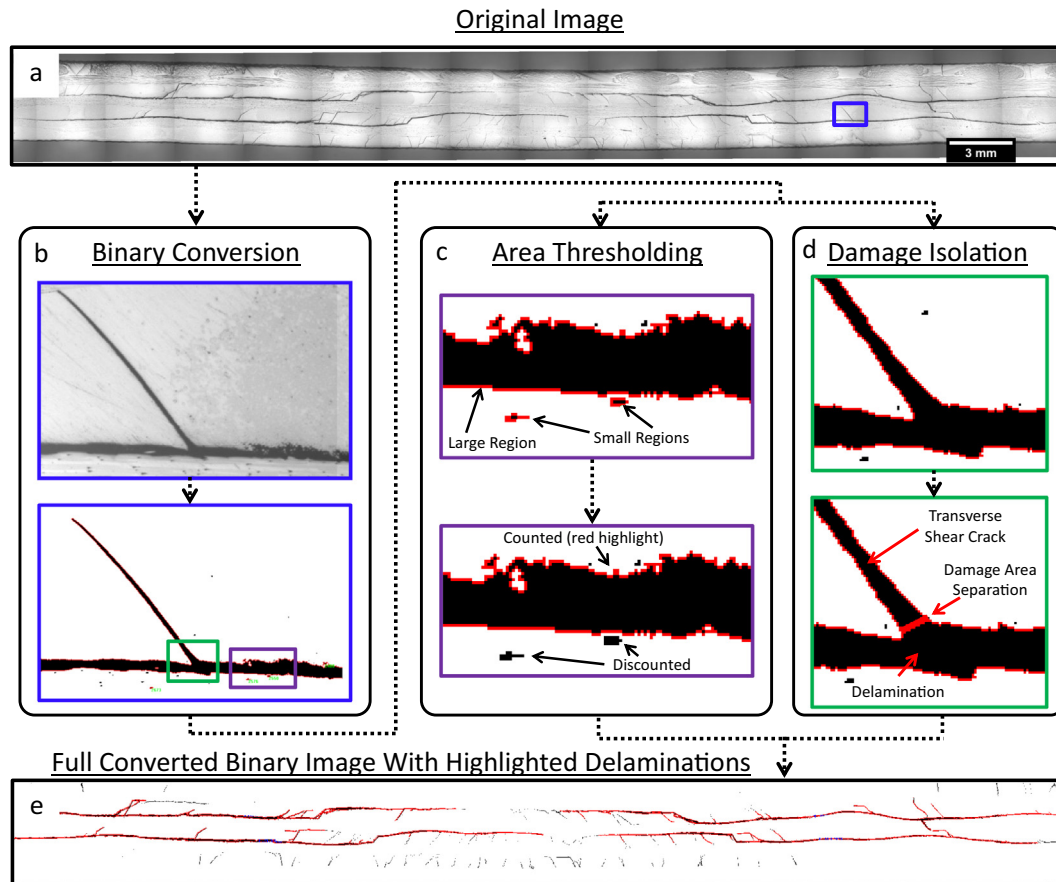


**Fig. 4.** Technique for isolating delamination damage from optical cross-sectional images. (a) Original tiled optical image. (b) Conversion of original image to binary using a half-intensity threshold filter. (c) Filtering of optical noise by removing groups of pixels with an area less than 0.01 mm<sup>2</sup>. (d) Manual isolation of delamination from transverse shear cracks. (e) Threshold image showing clearly defined delaminations and transverse shear cracks. (For interpretation of the references to colour in this figure legend, the reader is referred to the web version of this article.)

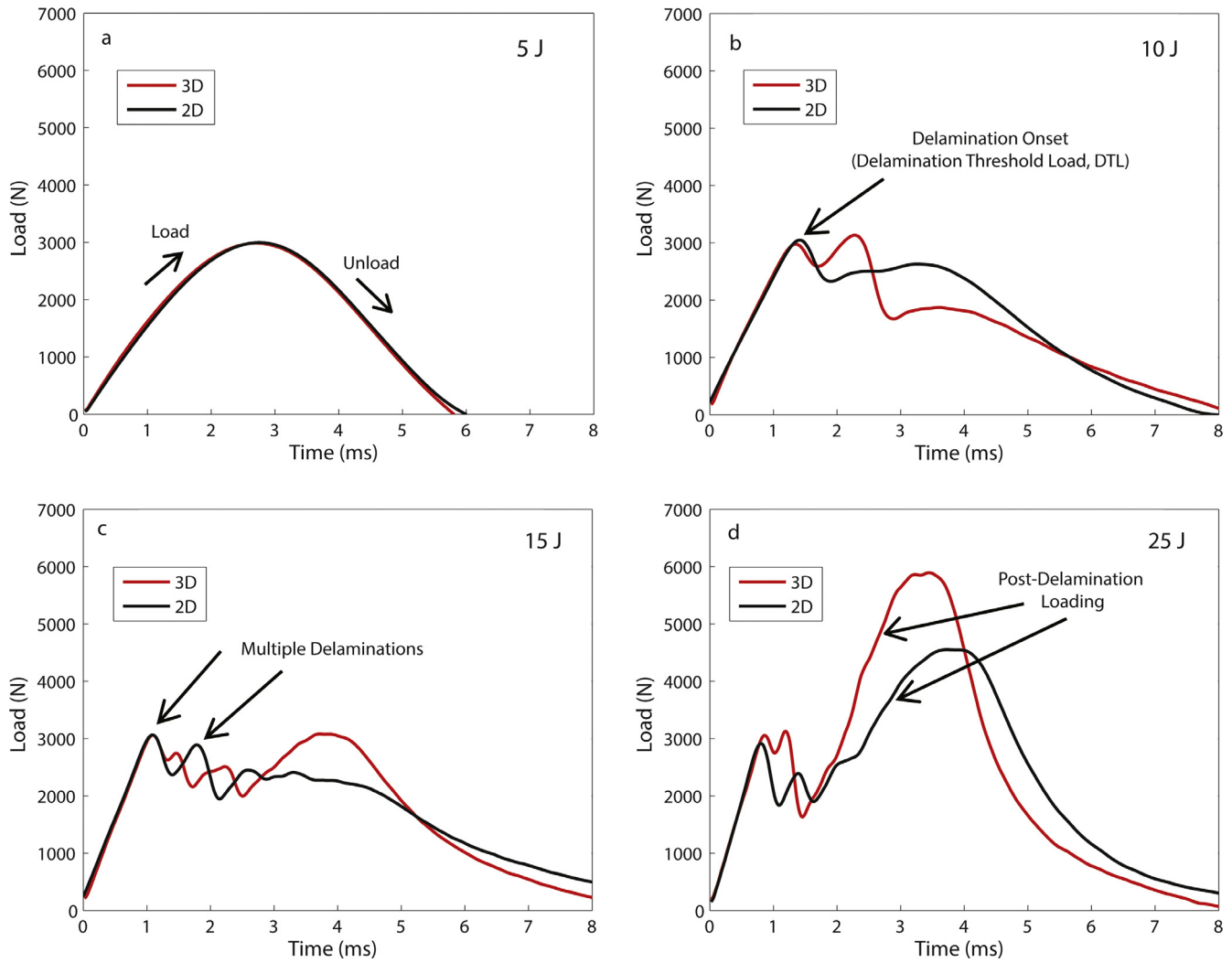


**Fig. 5.** Representative loading response of 2D and 3D beam specimens. (a) Elastic response for 2D and 3D specimens at 5.0 J of impact energy. (b) Impact response at 10.0 J. Delamination damage is introduced at the Delamination Threshold Load (DTL). (c) Impact response at 15.0 J shows multiple delamination events. (d) Impact response at 25.0 J. Loading above DTL occurs after the specimen is fully delaminated. (For interpretation of the references to colour in this figure legend, the reader is referred to the web version of this article.)

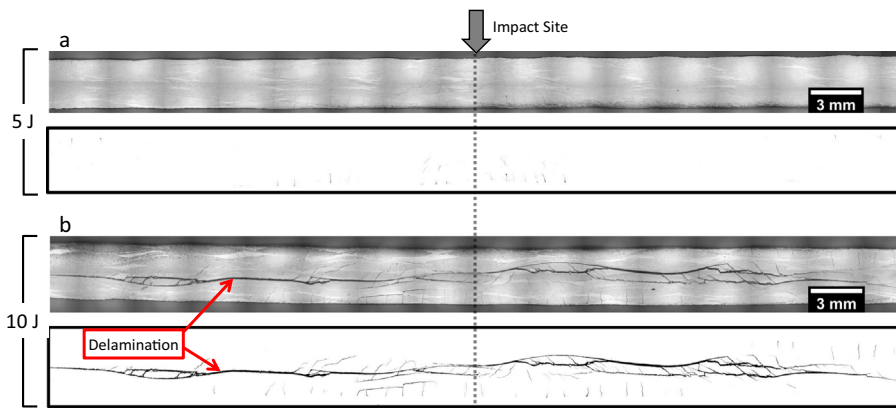


**Fig. 6.** Cross-sectional optical images and corresponding binary conversions of 2D beam specimens impacted at 5 J (a) and 10 J (b). Delamination damage occurs in samples impacted at 10 J but is absent in samples impacted at 5 J.

was counted as a shear crack if the damage occurred at an angle of between 30 and 60° with respect to the axis of impact, and if it traveled completely through at least one fabric layer.

#### 2.4. Damage volume calculations

Damage volume was estimated for both impacted beam and plate specimens. For beam samples, delamination opening was

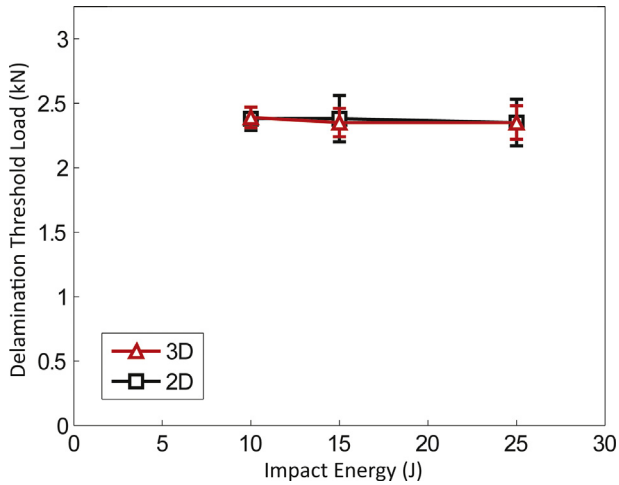


**Fig. 7.** Delamination threshold load (DTL) for 2D and 3D beam specimens subject to between 10 J and 25 J of impact energy. Error bars represent one standard deviation of 8 samples tested per impact energy. (For interpretation of the references to colour in this figure legend, the reader is referred to the web version of this article.)

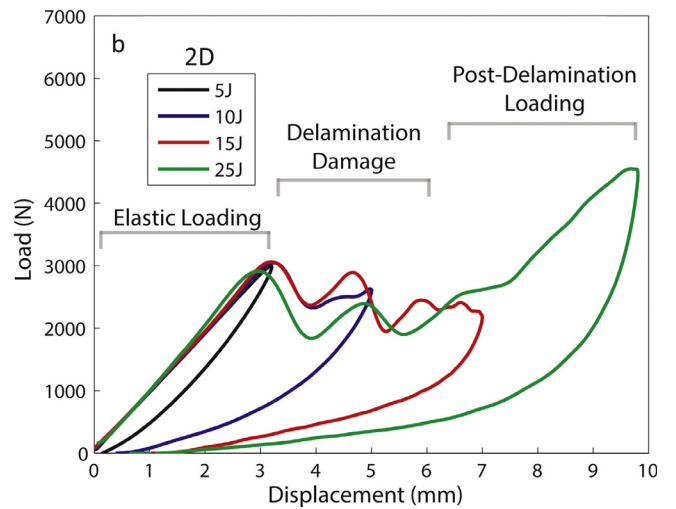
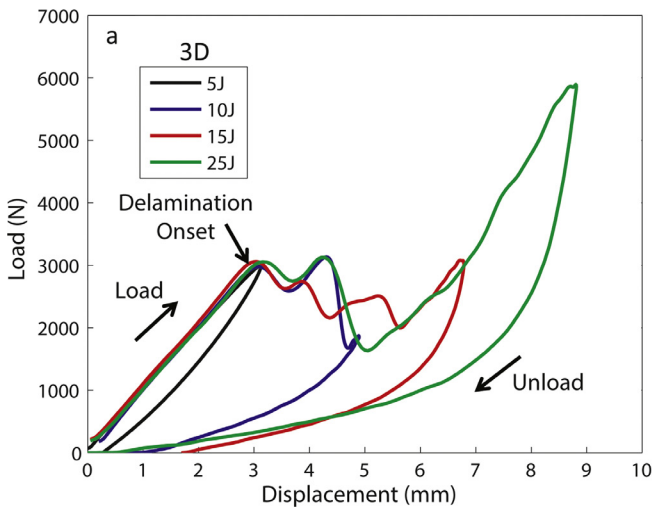


**Fig. 8.** Representative loading curves for beam specimens. (a) 3D beam specimens with onset of delamination denoted. (b) 2D specimens showing the three phases of loading: elastic, delamination damage, post-delamination. (For interpretation of the references to colour in this figure legend, the reader is referred to the web version of this article.)

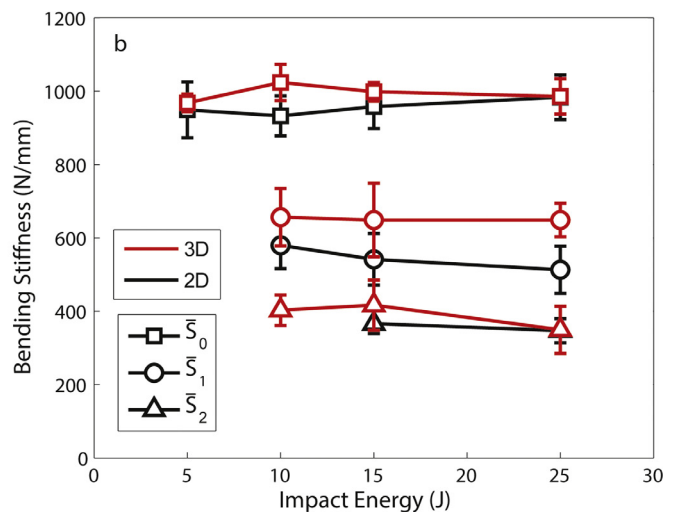
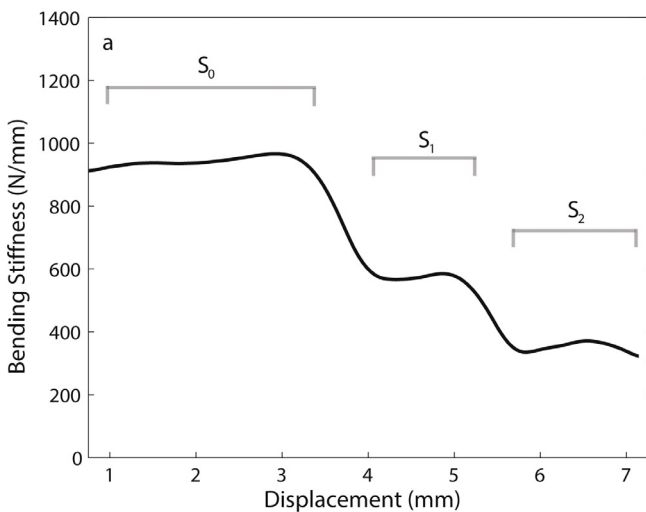


**Fig. 9.** Bending stiffness analysis of impacted composite beam specimens. (a) Instantaneous bending stiffness as a function of displacement for a representative 2D beam specimen subject to 15.0 J of impact energy. (b) Bending stiffness as a function of impact energy in all beam specimens. The reduction in bending stiffness is attributed to the formation of delaminations in the sample during impact. As this occurs, the stiffness reduces from the initial stiffness,  $S_0$ , to a final stiffness,  $S_n$ , where  $n$  is the number of delaminations present in the sample after impact. Error bars represent one standard deviation of at least 6 samples for each data point. (For interpretation of the references to colour in this figure legend, the reader is referred to the web version of this article.)

assumed to be constant through the width of the beam. Therefore, the damage volume,  $V_D^{beam}$ , was calculated by multiplying the average delamination opening of a longitudinal cross-section,  $\bar{A}_d^{beam}$ , by the width,  $w$ , of the beam:

$$V_D^{beam} = \bar{A}_d^{beam} w. \tag{3}$$

For plate specimens, the damage volume,  $V_D^{plate}$ , for each sample was calculated by assuming axisymmetric damage and sweeping the cross-sectional delamination opening of the plates about the axis of impact using (see derivation in Section S4 of Supplementary Information):

$$V_D^{plate} = \frac{\pi}{2} \left( \bar{A}_d^{plate} / \bar{L}_d^{plate} \right) \sum_{j=1}^n (r_o^2 - r_i^2)_j \tag{4}$$

where  $n$  is the number of disjoint delaminations in the cross-section,  $r_i$  and  $r_o$  are the shortest and farthest distances, respectively, from the axis of impact to any point of delamination  $j$ , and  $\bar{A}_d^{plate}$  and  $\bar{L}_d^{plate}$  are the calculated average delamination opening

and length of the cross-section, respectively. As will be shown later, the assumption of axisymmetric damage is largely satisfied (see Fig. 16). Variations in delamination length and opening about the impact point were, on average, less than 5%, except for in the warp direction of 3D woven composites, where increased delamination length was observed. These damage volume calculations are important for estimating the amount of healing agent required for self-healing [46] or determining the increase in water/solvent retention and permeability after impact.

### 3. Results and discussion

#### 3.1. Impact response of beams

Representative loading responses for 2D and 3D woven composite beam impact specimens is shown in Fig. 5. At 5.0 J of impact energy (Fig. 5a) both types of samples exhibit purely elastic loading and unloading. However, as impact energy increases to 10.0 J or more (Fig. 5b–d), a consistent drop in load is observed after the initial linear-elastic loading region. This drop in load is indicative of the conversion of internal strain energy to fracture energy through inter-ply delamination formation and propagation which span the length of the unclamped region. Reduction in the load with the introduction of delaminations is consistent with other studies on the impact response of plates and beams [42–45]. Cross-sectional images of two samples impacted at 5.0 J and 10.0 J clearly reveal large scale delamination damage in the 10.0 J case in contrast to the lack of any discernable damage in the 5.0 J case (Fig. 6). The load corresponding to the onset of delamination is defined as the Delamination Threshold Load (DTL) [42] and is plotted as a function of impact energy for both 2D and 3D woven composites in Fig. 7. Interestingly, the DTL is constant at approximately 3.1 kN regardless of the impact energy or fabric architecture. This indicates that the initiation of fracture damage is not significantly affected by the fabric architecture, but is likely controlled by properties of the matrix and the strength of the fiber-matrix interface.

As impact energy increases the number of delaminations increases, with up to 3 distinct delamination initiations and propagations occurring at the highest impact energy (25.0 J). In addition, for the 25.0 J case, the load exceeds the DTL after the last delamination event and the internal strain energy continues to build in the absence of the energy absorption provided by

delamination fracture. Load profiles for 2D and 3D samples match closely at all energies except in the post-delamination loading regime where the interlocked fabric architecture of 3D specimens provides inherent stiffening over the 2D composite architecture.

Load-displacement curves for 2D and 3D woven composite beam specimens are plotted in Fig. 8. The onset of delamination in both 2D and 3D woven composites occurs at approximately 3.1 kN. Further analysis reveals that the slope of the loading curve changes with the introduction of each delamination. The slope of the load-displacement curve is the bending stiffness,  $S$ , of the specimen during impact, defined as:

$$S_n = \left( \frac{\Delta P}{\Delta \delta} \right)_n \quad n \in [0, 1, 2] \quad (5)$$

where  $P$  is the load,  $\delta$  is the displacement, and  $S_n$  is the stiffness of the specimen containing  $n$  delaminations. Bending stiffness was

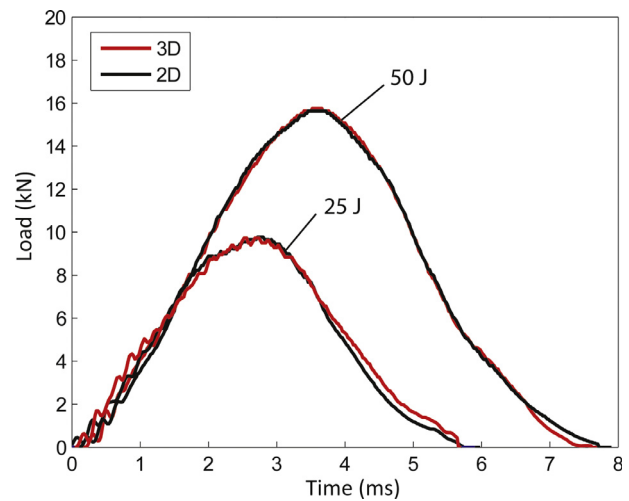


Fig. 11. Representative loading response of 2D and 3D plate specimens subject to 25.0 J and 50.0 J impact energy. Note: Loading for plate samples impacted at greater than 50.0 J of impact energy exceeded the capacity of the load cell and are not shown. (For interpretation of the references to colour in this figure legend, the reader is referred to the web version of this article.)

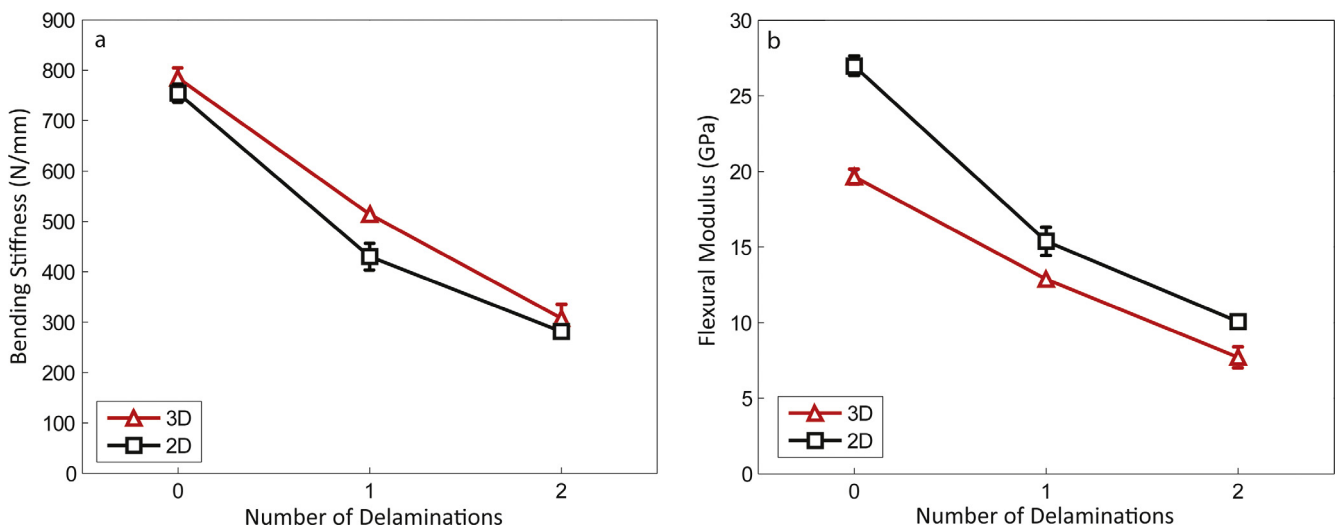
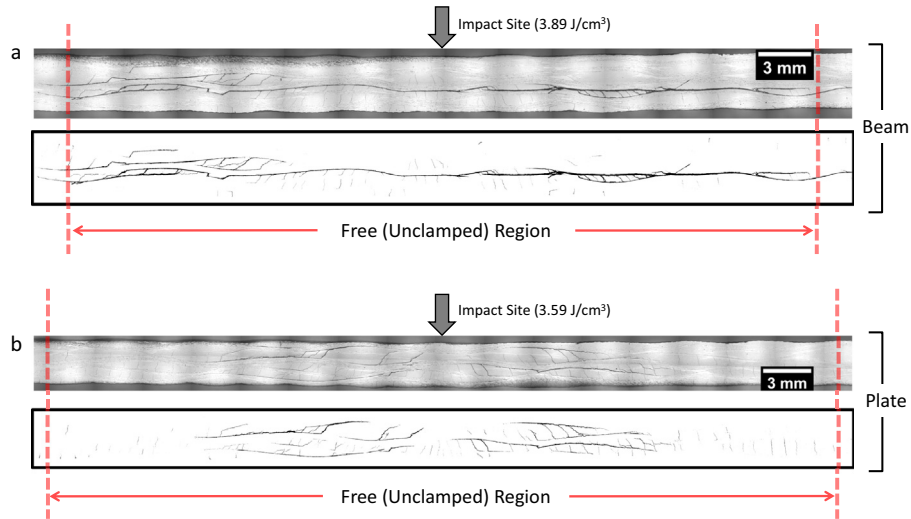
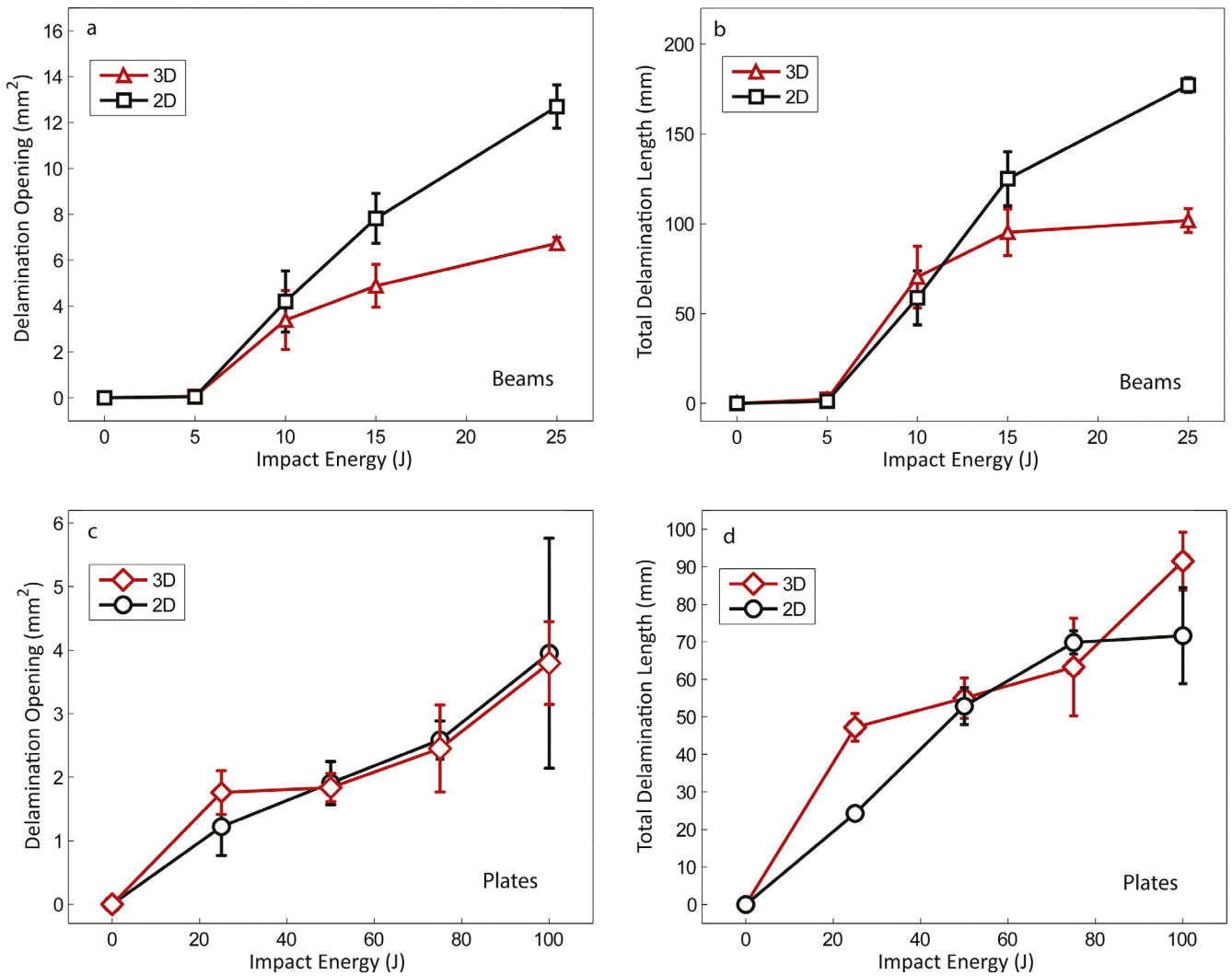


Fig. 10. Stiffness analysis of impacted composite beams as a function of delamination damage. (a) Bending stiffness for 2D and 3D beams as a function of number of delaminations. (b) Flexural modulus for 2D and 3D beams as a function of number of delaminations. Error bars represent one standard deviation. (For interpretation of the references to colour in this figure legend, the reader is referred to the web version of this article.)



**Fig. 12.** Optical cross-sections of impacted beam and plate specimens. (a) Cross-sectional image of a 2D beam specimen after a 10.0 J (3.89 J/cm<sup>3</sup>) impact. (b) Cross-sectional image of a 2D plate specimen after a 50.3 J (3.59 J/cm<sup>3</sup>) impact. Note: delamination damage in the beam specimen spans the entire unclamped region while delamination damage in the plate specimen does not. (For interpretation of the references to colour in this figure legend, the reader is referred to the web version of this article.)



**Fig. 13.** Delamination damage characterization for 2D and 3D composites. (a) Delamination opening plotted as a function of impact energy for beam specimens. (b) Total delamination length plotted as a function of impact energy for beam specimens. (c) Delamination opening plotted as a function of impact energy for plate specimens. (d) Total delamination length plotted as a function of impact energy for plate specimens. Error bars represent one standard deviation of at least 3 measurements for each data point. (For interpretation of the references to colour in this figure legend, the reader is referred to the web version of this article.)

averaged over each delamination domain to get an average bending stiffness for each delamination regime,  $\bar{S}_n$ .

Fig. 9a depicts the bending stiffness ( $S_n$ ) for a 3D beam specimen subject to 15.0 J of impact energy as a function of displacement. Three distinct regions ( $S_0$ ,  $S_1$ , and  $S_2$ ) are indicated; each is demarcated by the introduction of new delamination cracks. Fig. 9b shows the average value of the bending stiffness,  $\bar{S}_n$ , as a function of impact energy for both 2D and 3D composites subject to a range of impact energies. Notably, the average bending stiffness is constant for each class of composite and the reduction in stiffness with each delamination is consistent across a range of impact energies.

Fig. 10a presents the bending stiffness for both 2D and 3D specimens as a function of the number of delaminations, regardless of the level of initial impact energy. Remarkably, all the data collapses to a single correlation relation in which the reduction in bending stiffness scales with the number of delaminations. As delaminations are introduced, the original beam acts structurally like a combination of thinner beams with reduced cross-sectional moments of inertia.

Using classical beam theory and the calculated bending stiffness during impact, an estimate of the flexural modulus during each damage regime is made using:

$$E_n = \frac{L^3}{4wt^3} \left( \frac{P}{\delta} \right)_n = \frac{\bar{S}_n L^3}{4wt^3} \quad (6)$$

where  $E_n$  is the flexural modulus as the sample contains  $n$  delaminations,  $L$  is the unclamped length of the sample during impact,  $w$  is the sample width, and  $t$  is the sample thickness. The flexural modulus is plotted in Fig. 10b as a function of the number of delaminations. With no delaminations the flexural moduli for 2D and 3D composite samples during impact are 34.2 GPa and 24.9 GPa, respectively. Values of the flexural moduli correlate well to the flexural moduli obtained by quasi-static testing of undamaged samples (2D = 24.4 GPa; 3D = 19.9 GPa) [47], indicating that the flexural moduli of composite specimens can be estimated using bending stiffness data calculated during impact of beam specimens. While the bending stiffness as a function of the number of delaminations is consistent across the 2D and 3D architectures, 3D composites have a lower flexural moduli compared to 2D composites as a result of the lower fiber volume fraction and increased thickness of 3D composites.

### 3.2. Impact response of plates

Representative loading responses for 2D and 3D woven composite plates are plotted in Fig. 11. In contrast to beam specimens, the onset of delamination damage in the loading curve is not readily apparent during plate impact. Unlike beams, the delamination damage which occurs during plate impact does not span the entire unclamped damage region. Cross-sectional images of damaged beam and plate specimens are contrasted in Fig. 12. Delamination damage in the beam specimen clearly spans the entire unclamped region of the specimen, while delamination damage in the plate specimen does not. For this reason, flexural rigidity of the plate specimens in the unclamped region is preserved through a majority of the cross-section, and reductions in load from the introduction of delamination damage are not distinct.

### 3.3. Damage measurements

#### 3.3.1. Delamination opening and length

Delamination opening and length measurements for composite beams and plates sectioned along the warp direction (Z-tow travel direction) are provided in Fig. 13. Analysis of delamination damage

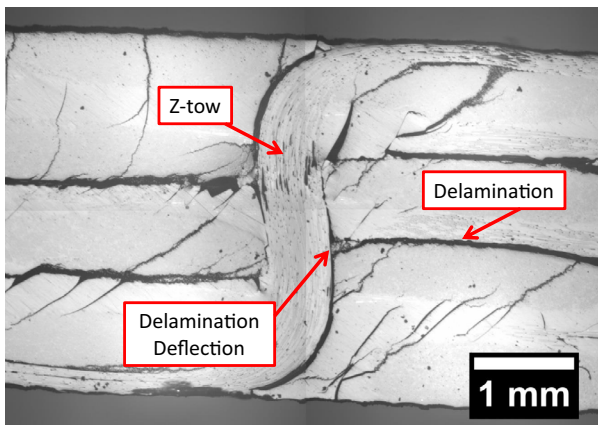


Fig. 14. Crack deflection in the vicinity of a through thickness Z-tow in a 3D composite beam specimen subject to 25.0 J of impact energy. (For interpretation of the references to colour in this figure legend, the reader is referred to the web version of this article.)

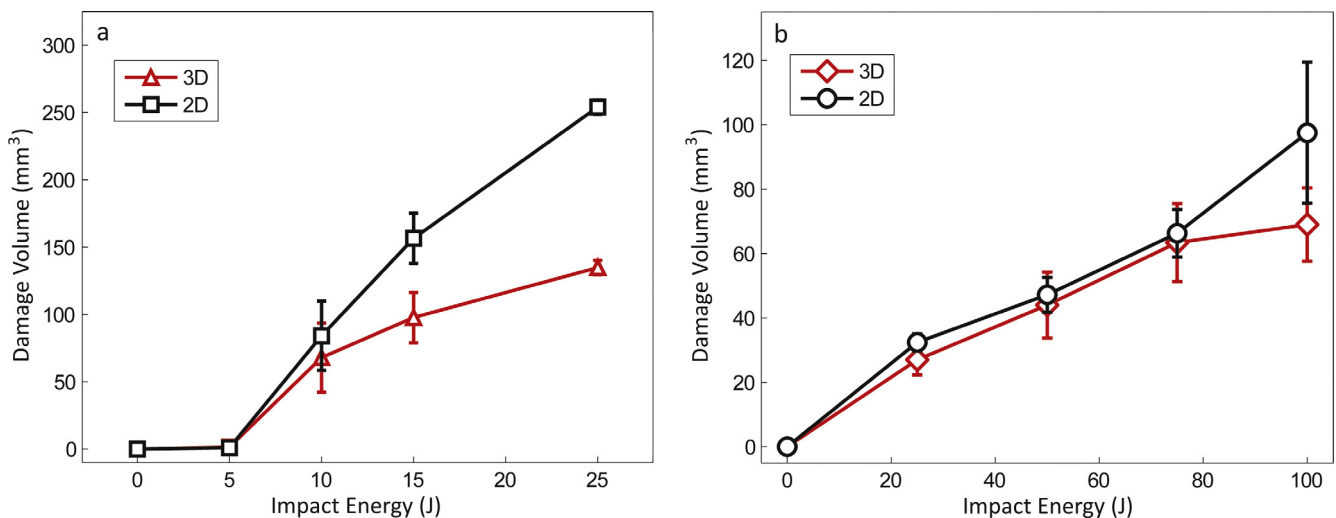


Fig. 15. Impact damage volume estimates for 2D and 3D composite beams and plates. (a) Damage volume of beam specimens as a function of impact energy. (b) Damage volume of plate specimens as a function of impact energy. Error bars represent one standard deviation of at least 3 measurements for each data point. (For interpretation of the references to colour in this figure legend, the reader is referred to the web version of this article.)

in 2D and 3D beam specimens (Fig. 13a and b) demonstrate that at the same impact energy, 2D composites exhibit larger total delamination opening and length after a critical impact energy (>5.0 J). Reduced delamination damage (length and opening) in 3D specimens is due to deflection of the delamination crack by the through thickness reinforcement tows (Fig. 14). Similar mechanisms have been observed in woven and stitched composites subject to out-of-plane impact [1,26–28]. Unlike beam specimens, 2D and 3D plate specimens do not exhibit major differences in the extent of delamination damage for any impact energy tested (Fig. 13c and d), possibly because there is not enough damage present to differentiate the two architectures. In beam specimens, noticeable differences in delamination openings and lengths for 2D and 3D composites impacted at the same energy are observed only after delamination openings exceed approximately  $4 \text{ mm}^2$  and delamination lengths exceed approximately 100 mm. Delamination openings and lengths for plate specimens do not exceed these values for either architecture.

### 3.3.2. Delamination damage volume

Delamination damage volume is plotted as a function of impact energy for impacted beams and plates is depicted in Fig. 15. As the impact energy increases, the damage volume increases for all specimens. The amount of damage volume in 3D composites is reduced when compared to 2D composites impacted at the same energy, though the effect is more pronounced in beam specimens. Reduced delamination volume in 3D specimens is a result of the deflection of delamination cracks and the lateral constraint offered by the through thickness reinforcement tows.

### 3.3.3. Ray analysis (Plates)

Optical images of back-face damage of 2D and 3D woven composite plates impacted at 50.3 J of impact energy are shown in Fig. 16a and b, respectively. Total delamination opening and length for 2D and 3D woven composite plates impacted at 50.3 J are reported in Fig. 16c and d, respectively. In 2D woven composites, no significant variations in the total delamination opening and

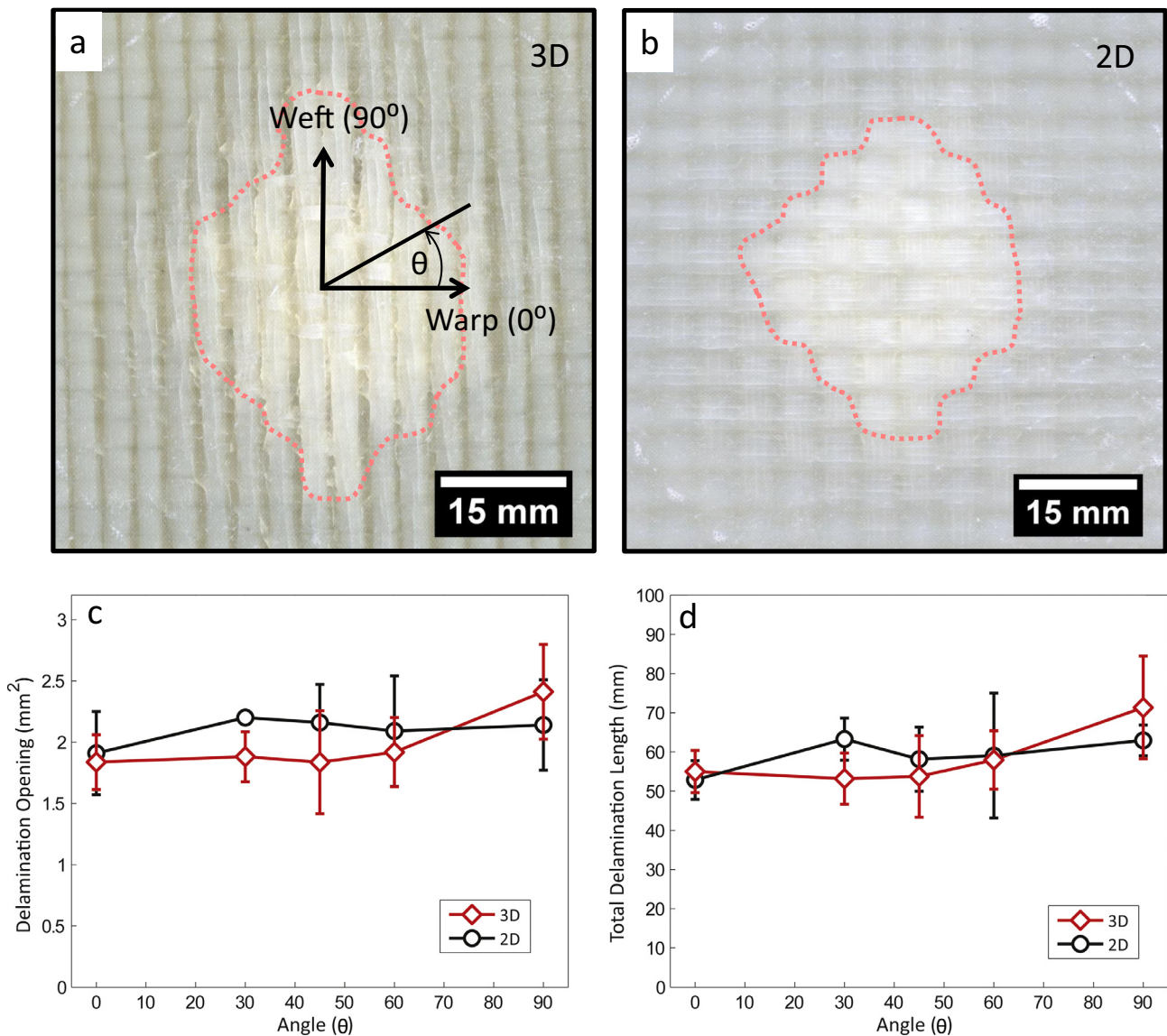


**Fig. 16.** Axial-symmetry analysis of impact damage in plate specimens. (a) Optical image of back face damage in 3D composite plate subject to 50.3 J of impact energy. Angular orientation ( $\theta$ ) for cross-sectional analysis is defined based on alignment with the warp direction. Approximate damage area is highlighted by a dashed red line. (b) Optical image of back face damage in a 2D composite plate subject to 50.3 J impact energy. Approximate damage area is highlighted by a dashed red line. (c) Delamination opening as a function of orientation angle. (d) Total delamination length as a function of orientation angle. Error bars represent the standard deviation of at least 3 measurements for each data point. (For interpretation of the references to colour in this figure legend, the reader is referred to the web version of this article.)

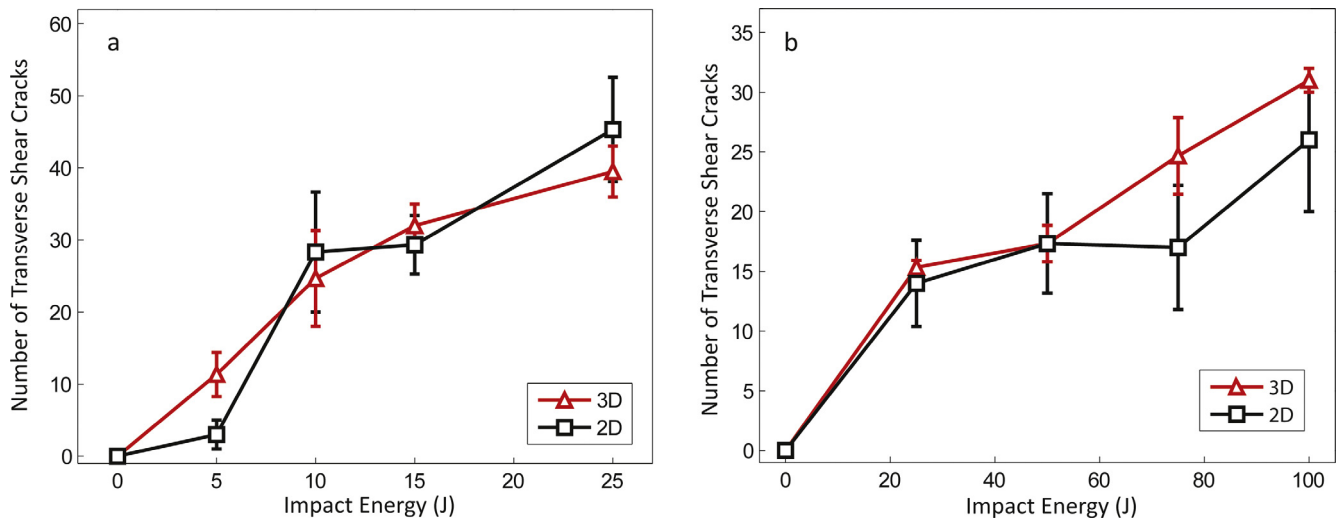


**Fig. 17.** Transverse shear cracks introduced by impact of 2D and 3D composite plates and beams. (a) Transverse shear cracks in the cross-sectional image of impacted beam specimens as a function of impact energy. (b) Transverse shear cracks in the cross-sectional image of impacted plate specimens as a function of impact energy. Error bars represent the standard deviation of at least 3 measurements for each data point. (For interpretation of the references to colour in this figure legend, the reader is referred to the web version of this article.)

length are observed as a function of bi-section angle. However, in 3D woven composites, the total delamination opening and length apices when the sample is sectioned through the weft direction ( $90^\circ$ ). Since the through thickness tows do not travel in the weft direction, delamination damage more freely propagates along the weft direction, leading to increased total delamination length and opening.

### 3.3.4. Shear crack analysis

The number of shear cracks present in the cross-sections of impact damaged composite as a function of impact energy is shown in Fig. 17. For both 2D and 3D plates and beams, as the impact energy increases the number of shear cracks increases. The number of cracks occurring is insensitive to the fabric architecture, indicating that unlike delamination damage, the number of shear cracks which occur during an impact is not affected by the presence of the Z-tow in the 3D fabric.

## 4. Conclusions

Impact damage in 2D and 3D woven composites was analyzed and compared across a range of impact energies. The threshold load to introduce delamination damage was found to be independent of the fabric architecture (2D vs. 3D) and impact energy, indicating that the onset of delamination is dominated by the properties of the matrix and fiber/matrix interface, despite 3D composites generally showing less delamination extent (length and opening) after damage initiation. Bending stiffness reduces with the introduction of delamination damage and the amount of reduction scales directly with the number of delaminations. In contrast to impact of beam specimens, plate impact results showed no indication of the initiation of delamination damage in the loading curve. Total delamination length and opening were consistently greater for 2D beam samples when compared to 3D beam samples impacted at the same energy, demonstrating that for low velocity impact, 3D composites are advantageous for reducing the total amount of damage. Ray analysis shows that total delamination length and opening does not vary as a function of fabric angle except in the weft direction of 3D composites where delamination deflection mechanisms provided by the Z-tows are not as operative. Additionally, the number of shear cracks which occur during

impact is independent of the fabric architecture. Data provided in this work can be used to predict total damage volume induced during impact and, ultimately, the reduction in strength and stiffness for an impacted composite.

## Acknowledgements

The authors gratefully acknowledge funding support from the Army Research Laboratory (grant number W911NF-14-2-003). We thank Mr. Gregory Milner, Mr. Lee Booher, and Mr. Stephen Mathine of the Aerospace Engineering Machine Shop for assistance in sample preparation, as well as Dr. David Farrow for assistance in calibrating drop-weight impact equipment.

## Appendix A. Supplementary data

Supplementary data associated with this article can be found, in the online version, at <http://dx.doi.org/10.1016/j.compositesa.2017.07.004>.

## References

- [1] Aymerich F, Priolo P. Characterization of fracture modes in stitched and unstitched cross-ply laminates subjected to low-velocity impact and compression after impact loading. *Int J Impact Eng* Jul. 2008;35(7):591–608.
- [2] Polimeno U, Meo M. Detecting barely visible impact damage detection on aircraft composites structures. *Compos Struct* 2009;91(4):398–402.
- [3] Liu D. Delamination resistance in stitched and unstitched composite plates subjected to impact loading. *J Reinf Plast Compos* 1990;9(1):59–69.
- [4] Strait LH, Karasek ML, Amateau MF. Effects of stacking sequence on the impact resistance of carbon fiber reinforced thermoplastic toughened epoxy laminates. *J Compos Mater* 1992;26(12):1725–40.
- [5] Hitchen SA, Kemp RMJ. The effect of stacking sequence on impact damage in a carbon fibre/epoxy composite. *Composites* 1995;26(3):207–14.
- [6] Fuoss E, Straznický PV, Poon C. Effects of stacking sequence on the impact resistance in composite laminates. Part 2: prediction method. *Compos Struct* 1998;41(2):177–86.
- [7] Fuoss E, Straznický PV, Poon C. Effects of stacking sequence on the impact resistance in composite laminates – Part 1: parametric study. *Compos Struct* 1998;41(1):67–77.
- [8] Lopes CS, Seresta O, Coquet Y, Gürdal Z, Camanho PP, Thuis B. Low-velocity impact damage on dispersed stacking sequence laminates. Part I: experiments. *Compos Sci Technol* 2009;69(7–8):926–36.
- [9] Lopes CS, Camanho PP, Gürdal Z, Maimí P, González EV. Low-velocity impact damage on dispersed stacking sequence laminates. Part II: numerical simulations. *Compos Sci Technol* 2009;69(7–8):937–47.

- [10] Cantwell W, Curtis P, Morton J. Post-impact fatigue performance of carbon fibre laminates with non-woven and mixed-woven layers. *Composites* 1983;14(3):301–5.
- [11] Jain LK, Mai Y-W. Mode I delamination toughness of laminated composites with through-thickness reinforcement. *Appl Compos Mater* 1994;1(1):1–17.
- [12] Dransfield KA, Jain LK, Mai Y-W. On the effects of stitching in CFRPs—I. mode I delamination toughness. *Compos Sci Technol* 1998;58(6):815–27.
- [13] Mouritz AP, Jain LK. Further validation of the Jain and Mai models for interlaminar fracture of stitched composites. *Compos Sci Technol* 1999;59(11):1653–62.
- [14] Tan KT, Watanabe N, Iwahori Y. Experimental investigation of bridging law for single stitch fibre using Interlaminar tension test. *Compos Struct* 2010;92(6):1399–409.
- [15] Iwahori Y, Nakane K, Watanabe N. DCB test simulation of stitched CFRP laminates using interlaminar tension test results. *Compos Sci Technol* 2009;69(14):2315–22.
- [16] Wood MDK, Sun X, Tong L, Katzos A, Rispler AR, Mai Y-W. The effect of stitch distribution on Mode I delamination toughness of stitched laminated composites – experimental results and FEA simulation. *Compos Sci Technol* 2007;67(6):1058–72.
- [17] Tan KT, Watanabe N, Sano M, Iwahori Y, Hoshi H. Interlaminar fracture toughness of vectran-stitched composites – experimental and computational analysis. *J Compos Mater* 2010.
- [18] Jain LK, Mai Y-W. Determination of mode II delamination toughness of stitched laminated composites. *Compos Sci Technol* 1995;55(3):241–53.
- [19] Jain LK, Dransfield KA, Mai Y-W. On the effects of stitching in CFRPs—II. Mode II delamination toughness. *Compos Sci Technol* 1998;58(6):829–37.
- [20] Wood MDK, Sun X, Tong L, Luo Q, Katzos A, Rispler A. A New ENF test specimen for the mode II Delamination toughness testing of stitched woven CFRP laminates. *J Compos Mater* 2007;41(14):1743–72.
- [21] Massabò R, Cox BN. Concepts for bridged Mode II delamination cracks. *J Mech Phys Solids* 1999;47(6):1265–300.
- [22] Massabò R, Mumm DR, Cox B. Characterizing mode II delamination cracks in stitched composites. *Int J Fract* 1998;92(1):1–38.
- [23] Rugg KL, Cox BN, Massabò R. Mixed mode delamination of polymer composite laminates reinforced through the thickness by z-fibers. *Compos Part Appl Sci Manuf* 2002;33(2):177–90.
- [24] Cox BN, Sridhar N. A Traction Law for Inclined Fiber Tows Bridging Mixed-Mode Cracks. *Mech Adv Mater Struct* 2002;9(4):299–331.
- [25] Massabò R, Cox BN. Unusual characteristics of mixed-mode delamination fracture in the presence of large-scale bridging. *Mech Compos Mater Struct* 2001;8(1):61–80.
- [26] Tan KT, Watanabe N, Iwahori Y. Effect of stitch density and stitch thread thickness on low-velocity impact damage of stitched composites. *Compos Part Appl Sci Manuf* 2010;41(12):1857–68.
- [27] Tan KT, Watanabe N, Iwahori Y. Impact damage resistance, response, and mechanisms of laminated composites reinforced by through-thickness stitching. *Int J Damage Mech* 2011.
- [28] Aymerich F, Pani C, Priolo P. Damage response of stitched cross-ply laminates under impact loadings. *Eng Fract Mech* 2007;74(4):500–14.
- [29] Mouritz AP, Cox BN. A mechanistic interpretation of the comparative in-plane mechanical properties of 3D woven, stitched and pinned composites. *Compos Part Appl Sci Manuf* 2010;41(6):709–28.
- [30] Bilisik K. Multi-axis three-dimensional weaving for composites: a review. *Text Res J* 2012;82(7):725–43.
- [31] Lee L, Rudov-Clark S, Mouritz AP, Bannister MK, Herszberg I. Effect of weaving damage on the tensile properties of three-dimensional woven composites. *Compos Struct* 2002;57(1–4):405–13.
- [32] Guess T, Reedy E. Comparison of interlocked fabric and laminated fabric Kevlar 49/epoxy composites. *J Compos Technol Res* 1985;7(4):136–42. <http://dx.doi.org/10.1520/CTR10310J>. ISSN: 0884-6804.
- [33] Tan P, Tong L, Steven GP, Ishikawa T. Behavior of 3D orthogonal woven CFRP composites. Part I. Experimental investigation. *Compos Part Appl Sci Manuf Mar.* 2000;31(3):259–71.
- [34] Quinn JP, McIlhagger AT, McIlhagger R. Examination of the failure of 3D woven composites. *Compos Part Appl Sci Manuf* 2008;39(2):273–83.
- [35] Coppola AM, Thakre PR, Sottos NR, White SR. Tensile properties and damage evolution in vascular 3D woven glass/epoxy composites. *Compos Part Appl Sci Manuf* 2014;59:9–17.
- [36] King S, Stewart G, McIlhagger AT, Quinn JP. Incremental damage development in a 3D woven carbon fibre composite. *Polym Polym Compos* 2007;15(7):521–33.
- [37] Rudov-Clark S, Mouritz AP. Tensile fatigue properties of a 3D orthogonal woven composite. *Compos Part Appl Sci Manuf Jun.* 2008;39(6):1018–24.
- [38] Baucom JN, Zikry MA. Low-velocity impact damage progression in woven E-glass composite systems. *Compos Part Appl Sci Manuf* 2005;36(5):658–64.
- [39] Baucom JN, Zikry MA, Rajendran AM. Low-velocity impact damage accumulation in woven S2-glass composite systems. *Compos Sci Technol Aug.* 2006;66(10):1229–38.
- [40] Baucom JN, Zikry MA. Evolution of failure mechanisms in 2D and 3D woven composite systems under quasi-static perforation. *J Compos Mater* 2003;37(18):1651–74.
- [41] Carlsson LA, Adams DF, Pipes RB. *Experimental Characterization of Advanced Composite Materials*. 4th Ed. CRC Press; 2014.
- [42] Schoepfner GA, Abrate S. Delamination threshold loads for low velocity impact on composite laminates. *Compos Part Appl Sci Manuf* 2000;31(9):903–15.
- [43] Kwon YS, Sankar BV. Indentation-flexure and low-velocity impact damage in graphite/epoxy laminates. *Mar.* 1992.
- [44] Davies GAO, Zhang X, Zhou G, Watson S. Numerical modelling of impact damage. *Composites May* 1994;25(5):342–50.
- [45] Davies GAO, Zhang X. Impact damage prediction in carbon composite structures. *Int J Impact Eng* 1995;16(1):149–70.
- [46] Patel AJ, Sottos NR, Wetzel ED, White SR. Autonomic healing of low-velocity impact damage in fiber-reinforced composites. *Compos Part Appl Sci Manuf* 2010;41(3):360–8.
- [47] Hart KR, Chia PXL, Sheridan LE, Wetzel ED, Sottos NR, White SR. Comparison of Compression-After-Impact and Flexure-After-Impact Protocols for 2D and 3D Woven Fiber-Reinforced Composites. *Compos Part A: Appl Sci Manuf* 2017. <http://dx.doi.org/10.1016/j.compositesa.2017.07.005>.